AFRL-RX-WP-JA-2017-0212

WINDOWING OF FULL WAVEFIELD DATA IIN MULTIPLE DOMAINS TO CHARACTERIZE ANGLE-BEAM SHEAR WAVE SCATTERING (POSTPRINT)

Yu Weng and Jennifer Michaels

Georgia Institute of Technology

19 September 2016
Interim Report

(STINFO COPY)

AIR FORCE RESEARCH LABORATORY
MATERIALS AND MANUFACTURING DIRECTORATE
WRIGHT-PATTERSON AIR FORCE BASE, OH 45433-7750
AIR FORCE MATERIEL COMMAND
UNITED STATES AIR FORCE

REPORT DOCUMENTATION PAGE

1. REPORT DATE *(DD-MM-YY)*	2. REPORT TYPE	3. DATES COVERED *(From - To)*
19 September 2016	Interim	3 March 2014 – 19 August 2016

4. TITLE AND SUBTITLE	5a. CONTRACT NUMBER
WINDOWING OF FULL WAVEFIELD DATA IIN MULTIPLE DOMAINS TO CHARACTERIZE ANGLE-BEAM SHEAR WAVE SCATTERING (POSTPRINT)	FA8650-10-D-5210-0014
	5b. GRANT NUMBER
	5c. PROGRAM ELEMENT NUMBER

6. AUTHOR(S)	5d. PROJECT NUMBER
Yu Weng and Jennifer E. Michaels – Georgia Institute of Technology	
	5e. TASK NUMBER 0014
	5f. WORK UNIT NUMBER X0GQ

7. PERFORMING ORGANIZATION NAME(S) AND ADDRESS(ES)	8. PERFORMING ORGANIZATION REPORT NUMBER
Georgia Institute of Technology, 311 Ferst Dr, Atlanta, GA 30332	

9. SPONSORING/MONITORING AGENCY NAME(S) AND ADDRESS(ES)	10. SPONSORING/MONITORING AGENCY ACRONYM(S)
Air Force Research Laboratory Materials and Manufacturing Directorate Wright-Patterson Air Force Base, OH 45433-7750 Air Force Materiel Command United States Air Force	AFRL/RXCA
	11. SPONSORING/MONITORING AGENCY REPORT NUMBER(S) AFRL-RX-WP-JA-2017-0212

12. DISTRIBUTION/AVAILABILITY STATEMENT
Distribution Statement A. Approved for public release: distribution unlimited.

13. SUPPLEMENTARY NOTES

14. ABSTRACT *(Maximum 200 words)*
Angle-beam ultrasonic inspection methods are frequently based on shear waves since they are readily generated using conventional longitudinal transducers and a wedge. Full wavefield imaging can be employed to measure such waves on the surface of a plate-like specimen after they have scattered from a feature or defect of interest, and multiple shear wave arrivals, or "skips," are readily visible due to beam spread [1]. Because of the complexity of the total wavefield, which also includes Rayleigh and longitudinal waves, it is challenging to experimentally quantify scattering from the primary skip of interest. Considered here is a methodology to isolate shear wave scattering from a through-hole caused by a specific shear wave skip that is incident upon the hole. First, the residual wavefield is obtained by performing wavefield baseline subtraction before and after the introduction of a scatterer [2]. Next, a 3-D Fourier transform is performed to convert the residual signals in the time and space domain (t-x-y) to the frequency-wavenumber domain (ω-kx-ky).

15. SUBJECT TERMS
Scattering, Ultrasonography, Spatial filtering, Ultrasonic scattering, Scattering measurement, Rayleigh, Longitudinal wave

16. SECURITY CLASSIFICATION OF:			17. LIMITATION OF ABSTRACT:	18. NUMBER OF PAGES	19a. NAME OF RESPONSIBLE PERSON (Monitor)
a. REPORT Unclassified	b. ABSTRACT Unclassified	c. THIS PAGE Unclassified	SAR	11	Eric Lindgren 19b. TELEPHONE NUMBER *(Include Area Code)* (937) 255-9806

Windowing of Full Wavefield Data in Multiple Domains to Characterize Angle-Beam Shear Wave Scattering

Yu Weng and Jennifer E. Michaels [a)]

School of Electrical and Computer Engineering,
Georgia Institute of Technology, Atlanta, GA 30332-0250, USA

[a)] Corresponding author: jemichaels@gatech.edu

Abstract. Angle beam ultrasonic inspection methods are frequently based on shear waves that are generated using conventional longitudinal transducers and a wedge. Full wavefield imaging can be employed to measure such waves on the surface of a plate-like specimen after they have scattered from a feature or defect of interest, and multiple shear wave arrivals, or "skips," are readily visible due to beam spread. Because of the complexity of the total wavefield, which also includes Rayleigh and longitudinal waves, it is challenging to experimentally quantify scattering from the primary skip of interest. Proposed here is a methodology to isolate shear wave scattering from a through-hole caused by a specific shear wave skip. By combining 3-D Fourier filters and space-time windows, the forward and backward scattering can be readily quantified as a function of measurement direction. Results are shown for several hole sizes of interest.

INTRODUCTION

In the field of ultrasonic nondestructive evaluation (NDE), one research topic of interest is to isolate, characterize and quantify scattering from known types of damage to improve the reliability and accuracy of NDE methods. Ultrasonic NDE of fastener holes is of particular interest for aerospace structures since these holes are a site of fatigue cracks. One common technique for fastener hole NDE in plate-like structures is shear wave inspection using the angle-beam technique [1], which is the method considered here. Angle-beam shear waves are generated with a longitudinal piezoelectric transducer mounted on a wedge to refract incident longitudinal waves past the first critical angle [2].

Detailed characterization of ultrasonic scattering from an undamaged through-hole is considered using full wavefield data acquired on the plate surface before and after introducing the hole [3]. There are two main challenges for quantifying shear wave scattering from the hole. The first is how to extract shear components from the total wavefield. Although the incident and scattered wavefield consists mainly of shear waves, both Rayleigh and longitudinal waves are also present. The second challenge is how to separate the scattered waves due to the primary incident shear wave "skip" from the quite complicated total wavefield, which includes as many as four shear skips.

The methodology presented here combines 3-D frequency-wavenumber filtering with space-time windowing to isolate and quantify shear wave scattering from a through-hole resulting from the primary incident skip. Results are shown as plots of energy vs. angle at different times.

EXPERIMENTAL SETUP

Wavefield data are recorded on the top surface of a mirror-finish aluminum plate using a laser Doppler vibrometer mounted on an XYZ scanner, which measures out-of-plane wave motion. The size of the plate is 305 mm × 305 mm × 6.35 mm and the scan area is 30 mm × 30 mm with a spatial increment of 0.25 mm in both the *x* and *y* directions. Details of the experimental procedures can be found in [3]. The incident wavefield is obtained by a

5 MHz center frequency transducer and an angle-beam shear wedge at a nominal refracted angle of 56.8° in aluminum, and the excitation is a large-amplitude spike. Here, the scatterer is a cylindrical through-hole. As shown in Fig. 1, the nominal point of beam incidence is defined as the origin in the x-y plane and the hole is placed at a distance of 1.5 skips from the origin to maximize scattered waves from where the hole penetrates the back surface of the plate. Note that one skip or V-path refers to a path of incident waves propagating from the top surface, reflecting from the bottom surface, and returning to the top surface; Eq. (1) gives the coordinate y_c corresponding to 1.5 skips at the nominal refracted angle θ_{r_nom} where h is the plate thickness and d is the hole diameter.

$$y_c = 3h \cdot \tan \theta_{r\_nom} + d/2. \tag{1}$$

Only the top surface motion is measured by the LDV, so the apparent shear phase velocity projected onto the surface is not the bulk wave speed c_s but is a function of the actual refracted angle θ_r:

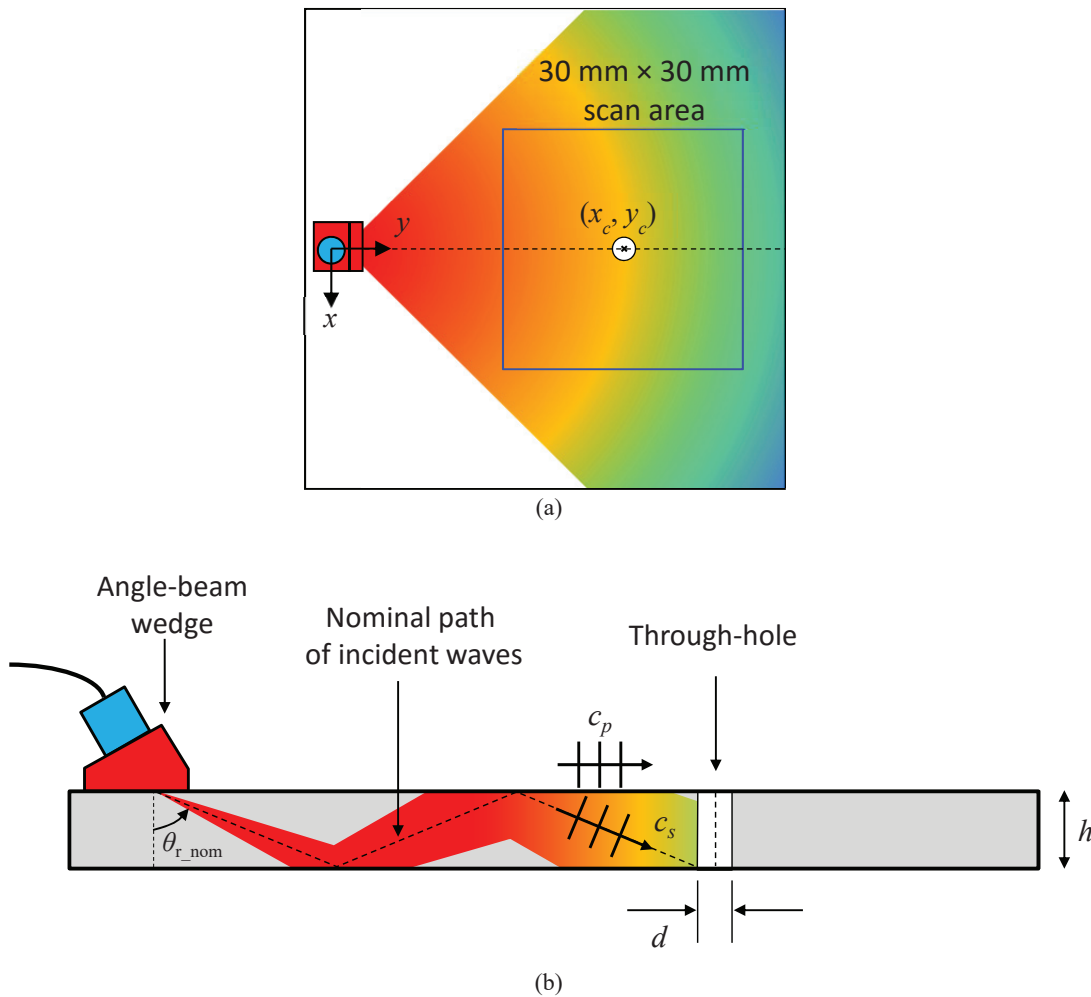$$c_p = \frac{c_s}{\sin \theta_r}. \tag{2}$$

(a)

(b)

FIGURE 1. Experimental setup for the acquisition of angle-beam wavefields in an aluminum plate with a through-hole. (a) Top view, and (b) side view (not to scale).

METHODOLOGY

The proposed methodology is illustrated by quantifying scattered waves from a 3.18 mm diameter, air-filled through-hole. Three main techniques are applied here: (1) wavefield baseline subtraction removes most of the incident waves and isolates the scattered waves; (2) shear wave filtering extracts shear components from the total wavefield; and (3) scattered shear skip windowing tracks and filters the primary skip of the shear scattered waves from all observed shear waves.

Wavefield Baseline Subtraction

Wavefield baseline subtraction aims to remove incident waves to separate waves scattered from the hole. The strategy is to fix the current wavefield with the hole and find an optimal shifted baseline wavefield without the hole to get the minimal residual after subtraction by aligning incident waves below the hole. Specifically, both the baseline and current wavefield data are first transformed to the frequency-wavenumber domain (ω, k_x, k_y) via a 3-D Fourier transform. Then, $+k_y$ filtering is applied to extract forward propagating waves. Next, wavefield data are reconstructed in the time-space domain (t,x,y) via an inverse Fourier transform. Then, spatial windowing is used to isolate only incident waves below the hole. Next, global space-time alignment (GSTA) [4], is performed to obtain the optimal shifts $(\Delta t, \Delta x, \Delta y)$ for the baseline wavefied by aligning incident waves extracted from the baseline and current wavefields. These shifts are applied to total (unfiltered) baseline wavefield prior to baseline subtraction. The final step is to compensate any amplitude differences between the current and shifted baseline wavefields by scaling the baseline wavefield to minimize the mean square error after subtraction.

The wavefield baseline subtraction procedure is summarized as follows:

- Smooth the data along the t, x and y axes to avoid edge effects in the Fourier domain.
- Apply spatial windowing to remove the through-hole noise.
- Take the 3-D Fourier transform: $w(t,x,y)\xrightarrow{\mathcal{F}}W(\omega,k_x,k_y)$.
- Apply k_y filtering ($k_y > 0$) to extract forward propagating waves:
  - Smooth and filter the data in frequency to minimize spatial aliasing.
  - Filter and smooth the data along the k_y axis for $k_y > 0$.
- Take the inverse 3-D Fourier transform: $W_{k_y>0}(\omega,k_x,k_y)\xrightarrow{\mathcal{F}^{-1}}w_{\text{forward}}(t,x,y)$.
- Apply spatial windowing to isolate incident waves below the hole.
- Use GSTA to get the optimal shifted baseline wavefield: $\hat{w}_B(t,x,y)=w_B(t+\Delta t, x+\Delta x, y+\Delta y)$.
- Compensate amplitude differences by minimizing mean squared error of two sets of wavefield data using the calculated compensation coefficient α,

$$\alpha = \frac{\sum\limits_{t,x,y} w_C \cdot \hat{w}_B}{\sum\limits_{t,x,y} \hat{w}_B^2}. \tag{3}$$

- Calculate the residual wavefield $w_R(t,x,y)$,

$$w_R(t,x,y)=w_C(t,x,y)-\alpha \cdot w_B(t+\Delta t, x+\Delta x, y+\Delta y). \tag{4}$$

Figure 2(a) shows a typical wavefield snapshot prior to $+k_y$ filtering. Figure 2(b) shows the corresponding snapshot after $+k_y$ filtering; the green rectangle indicates the spatial window used to align the current and baseline wavefields and thus obtain the offsets Δt, Δx, and Δy. All subsequent analysis steps are applied to the residual wavefield, $w_R(t,x,y)$.
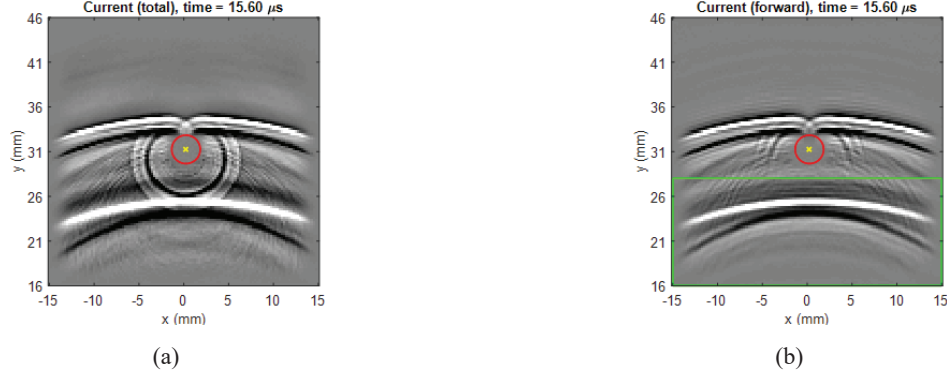
FIGURE 2. Snapshot of the current wavefield at 15.60 μs (a) before and (b) after $+k_y$ filtering. The green rectangular box indicated the spatial window used for wavefield alignment.

Shear Wave Filtering

Shear waves are the main waves of interest for the inspection method being considered here. However, both Rayleigh and longitudinal waves are also present. Shear wave frequency-wavenumber filtering is applied to extract the shear contribution from the total wavefield. Frequency-wavenumber filtering has been applied to separate guided wave modes using the appropriate dispersion curves [5,6]. Here, the idea is to make use of the difference in phase velocity between these shear, longitudinal and Rayleigh waves to build a 3-D frequency-wavenumber filter to extract shear components in the Fourier domain. The filtered shear wavefield is then reconstructed by taking the inverse 3-D Fourier transform.

Firstly, 3-D wavefield data are transformed from the time-space domain (t,x,y) to the frequency-wavenumber domain (ω,k_x,k_y) via a 3-D Fourier transform. As shown in Fig. 3(a), the 3-D data appear cone-like in the ω-k_x-k_y domain. Figure 3(b) shows a k_x-k_y slice at $f = 5$ MHz, and Fig. 3(c) shows a k_r-f slice for the specific propagation direction of 90°. According to the well-known relation between phase velocity, frequency and wavenumber,

$$c_p = \frac{\omega}{k_r}, \tag{5}$$

for the k_x-k_y slice, given a specific frequency value, a constant phase velocity corresponds to a circle of a constant radius and larger phase velocities correspond to smaller circles; for the k_r-f slice, a constant phase velocity corresponds to a line of a constant slope and larger phase velocities correspond to steeper lines. Therefore, phase velocity becomes the key to understanding how wavefield data distribute in the Fourier domain.
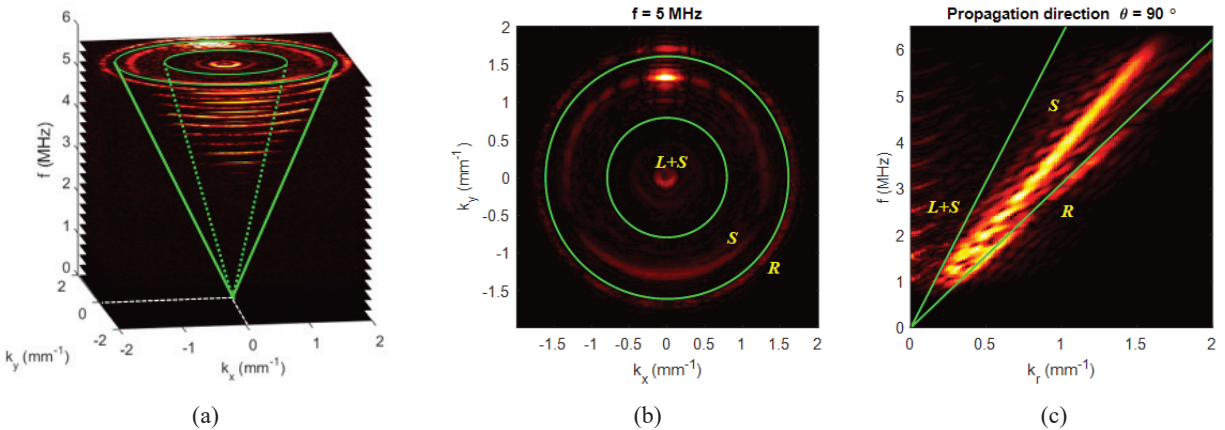

FIGURE 3. Wavefield data in (a) the 3-D frequency-wavenumber domain, (b) a k_x-k_y slice, and (c) a k_r-f slice.

Secondly, phase velocity ranges must be appropriately set for wave mode separation. Nominal wave speeds of Rayleigh, shear and longitudinal waves are 2.9, 3.1 and 6.3 mm/µs, respectively. The measured phase velocity of Rayleigh waves is the same as the nominal Rayleigh wave speed since the measurement surface guides the Rayleigh wave. However, phase velocities of both shear and longitudinal waves do not correspond to the nominal wave speeds but are functions of the refracted angle as given by Eq. (2). Since $\sin\theta_r$ is always between 0 and 1, the shear wave phase velocity cannot be smaller than 3.1 mm/µs. Similarly, the longitudinal wave phase velocity cannot be smaller than 6.3 mm/µs. Even though there is a phase velocity ambiguity between shear waves with shallow refracted angles and longitudinal waves with steep refracted angles, it is still helpful to separate each wave mode by setting phase velocity ranges as summarized in Table 1.

TABLE 1. Phase velocity ranges for wave mode separation

Wave Mode	Wave speed (mm/µs)	Phase Velocity (mm/µs)	Phase Velocity Range (mm/µs)
Rayleigh	2.9	2.9	2-3.1
Shear	3.1	>3.1	3.1-6.3
Longitudinal	6.3	>6.3	6.3-∞

Thirdly, a 3-D Fourier filter is built based on the shear phase velocity range. For each frequency, there is an associated k_x-k_y slice, and the two bounds of shear wave phase velocities correspond to two circles as shown in Fig. 3(b) for the frequency of 5 MHz. Then, pure shear components can be extracted in the frequency-wavenumber domain by multiplying each k_x-k_y slice with a 2-D "donut" filter (in practice the filter is smoothed by a 33% radial Tukey window). Finally, shear wavefield data in the time-space domain are reconstructed via an inverse 3-D Fourier transform. Figure 4 shows a series of wavefield snapshots before and after shear wave filtering, and it is instructive to see the resulting simpler images after the Rayleigh and longitudinal waves are almost completely removed.
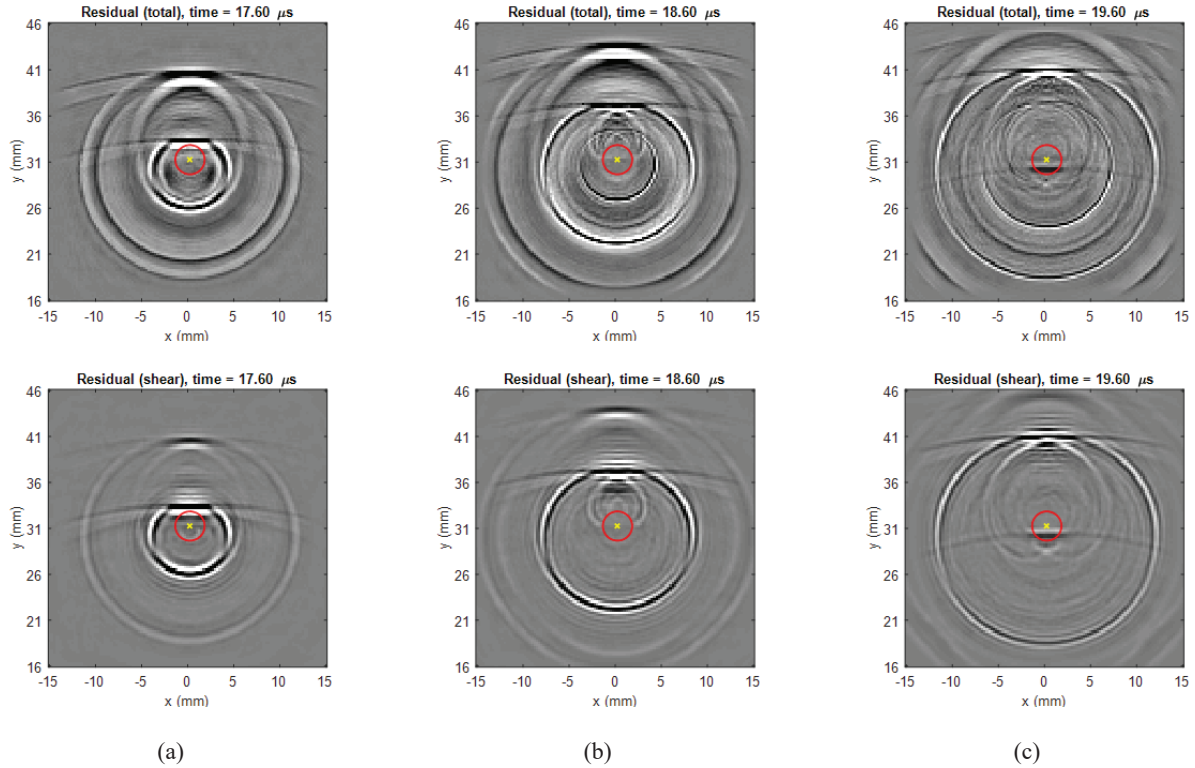

(a)   (b)   (c)

FIGURE 4. Snapshots of the residual wavefield before and after shear wave filtering. (a) 17.6 µs, (b) 18.6 µs, and (c) 19.6 µs.

Scattered Shear Skip Windowing

Based on the current experimental setup and scan area, four skips of shear waves can be observed in the total wavefield due to beam spread. Referring to Fig. 1(b), the transducer is positioned 1.5 skips from the hole, meaning that the second skip as measured on the surface will be most affected by the scattering of the incident wave by the hole. Scattered shear skip windowing is accomplished to get a direct quantification of scattering based on the second skip of shear waves in the time-space domain. It is straightforward and helpful to build insight of how the energy of the scattered shear wave evolves combined with the corresponding snapshot of wavefield data as time increases. So the purpose is to extract the second shear skip from all four observed shear wave skips.

Ray tracing analysis is performed to track both the incident waves and the scattered waves. One assumption is that incident wavefronts are circular in the x-y plane. The objective is to perform approximate ray tracing that matches observed incident and scattered waves; i.e. find the time-dependent propagating radii for both incident and scattered waves, r_{inc} and r_{scat}, for each incident ray. Figure 5 illustrates the ray tracing process.

Given the geometric information shown in Fig. 5(a), which includes the transducer location, the hole center and radius, all incident rays can be sorted into rays that hit the hole and rays that miss the hole. As shown in Fig. 5(b) for the second shear wave skip propagating from the side view, given a specific snapshot time value, t_{snap}, the radius r_{inc} of the incident wave can be calculated as,

$$r_{inc} = \sqrt{(t_{snap} - t_{wedge})^2 c_s^2 - (4h)^2} , \qquad (6)$$

where t_{wedge} is the time for the longitudinal wave to propagate through the wedge.

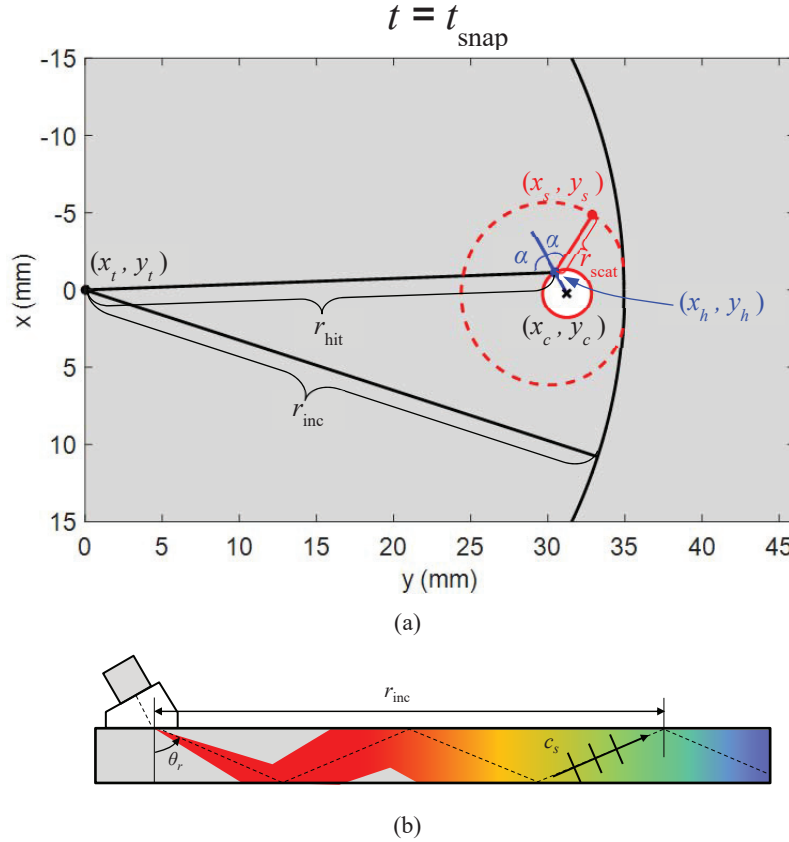**FIGURE 5**. Illustration of ray tracing analysis at $t=t_{snap}$ (not to scale). (a) Calculated trajectories of second skip of shear incident and scattered waves. (b) Side view of incident waves propagating in the plate.

For tracking the scattered waves resulting from the second skip, two questions should be answered: given a specific incident ray, (1) when does the corresponding reflected (scattered) ray begin to propagate from the hitting point, and (2) which direction does that ray follow after hitting the hole. Given a specific incident ray that hits the hole, the distance between the source and the hitting point, r_{hit}, can be readily calculated. The corresponding time for hitting the hole, t_{hit}, is calculated by inverting Eq. (6):

$$t_{hit} = t_{wedge} + \frac{\sqrt{r_{hit}^2 + (4h)^2}}{c_s}.$$

(7)

The reflected (scattered) direction can also be calculated based on the assumption of a specular reflection at the hitting point on the hole, which is illustrated in Fig. 5(a) for an angle of α with respect to the normal vector. Based on the analysis shown here for one incident ray, the relation of t_{hit} and the reflected directions can be built for all incident rays that hit the hole. Once the given t_{snap} is larger than t_{hit}, which means that scattered waves begin to propagate for the ray of interest, the radius of the propagating scattered waves based on each reflected ray is tracked by using the nominal shear phase velocity, c_{p_nom},

$$r_{scat} = c_{p\_nom}(t_{snap} - t_{hit}).$$

(8)

Then, an entire trajectory of scattered waves is readily built by combining the reflected directions and all corresponding r_{scat}. As shown in Fig. 6, calculated trajectories of the incident and scattered second skip shear waves match well with the experimental residual wavefield at different snapshot times.

Based on this procedure for wave trajectory tracking, a space-time filter is constructed by setting an appropriate ring width Δr for both the incident and scattered wave trajectories (r_{inc} and r_{scat}) to make it reasonably include the second shear skip of incident and scattered waves (note that the incident trajectories are used only for tracking forward scattered waves in the shadow region). The two edges around the ring-like filter are smoothed by a radial Tukey window. The scattered second shear skip is finally extracted by multiplying the space-time filter along the time axis. An example snapshot before and after space-time filter windowing is shown in Fig 7.

Scattering Pattern Generation

Scattering is quantified as scattered energy versus measurement direction for a specific snapshot. The measurement direction θ is relative to a reference point, which here is taken to be the hole center. 0° is defined as the measurement direction horizontally to the right, and thus 90° and 270° refer to the vertically forward and backward measurement directions, respectively. The scattered second shear skip wavefield is radially interpolated outward from the hole center along a line defined by θ. Given a snapshot and a specific measurement direction, scattered energy is calculated by summing squared amplitude values along that direction.
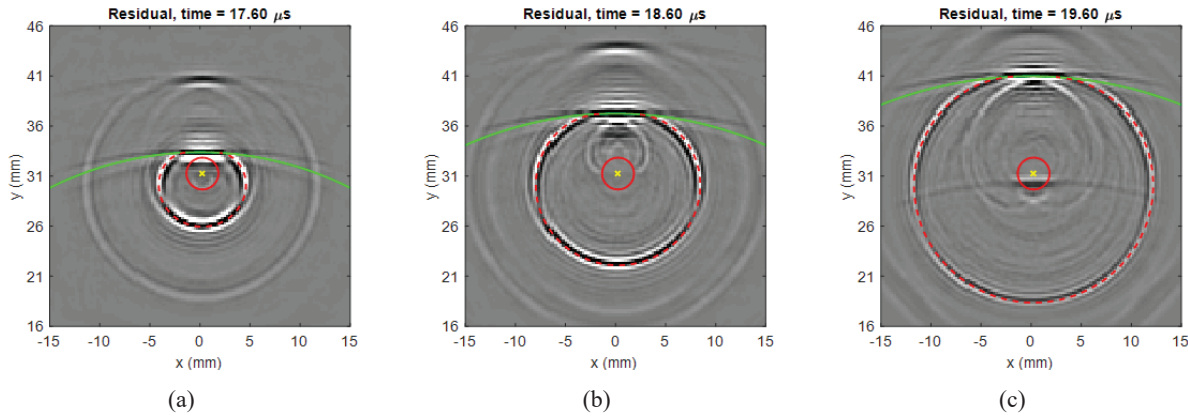

(a)   (b)   (c)

FIGURE 6. Snapshots of residual wavefield with calculated trajectories of the second skip of shear incident and scattered waves at (a) 17.6 μs, (b) 18.6 μs and (c) 19.6 μs.
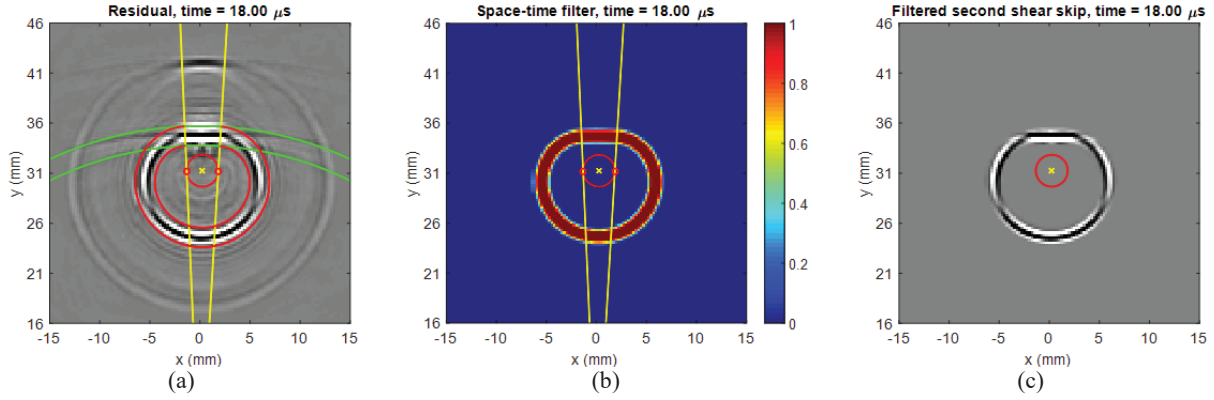
FIGURE 7. Scattered shear skip windowing at 18 μs. (a) Snapshot of residual wavefield marked with the space-time filter. (b) Space-time filter smoothed by a radial Tukey window. (c) Snapshot of filtered second skip of scattered shear waves.

The scattering is not a single curve but a group of curves, each with a specific snapshot time. As can be seen for the snapshot analyzed in Fig. 8, the energy of forward and backward scattered waves is distributed approximately symmetrically about 90° and 270°, respectively (i.e., about the *y* axis), and forward scattering is stronger than backscattering. There is an obvious angle range of scattered waves around 90° between two local minima that bound the shadow region where most of the incident waves are blocked by the hole. These minima, which are located at approximately 60° and 120°, mark the transition between forward scattering and the shadow region. There are also two minima bracketing the backscattered region located at approximately 205° and 335°. These minima correspond to a phase change, which can be seen in the snapshot of Fig. 8(a).

RESULTS

The quantification method presented here can also be applied to different hole sizes and results are shown in Fig. 9. Generally, for all three holes, forward scattering is stronger than backscattering, which means that the energy difference of forward scattered waves caused by the shadowing effect is larger than the total energy of backscattered waves. Specifically, it is clear to see how the energy distribution of scattered waves evolves as time increases for each hole size. For all three holes, there is a decaying trend of backscattered energy as time progresses, which is expected because of beam spread. For forward scattering, there is a generally increasing trend with time, likely caused by the diffracted waves reforming in the shadow region behind the hole. Comparing curves for the three
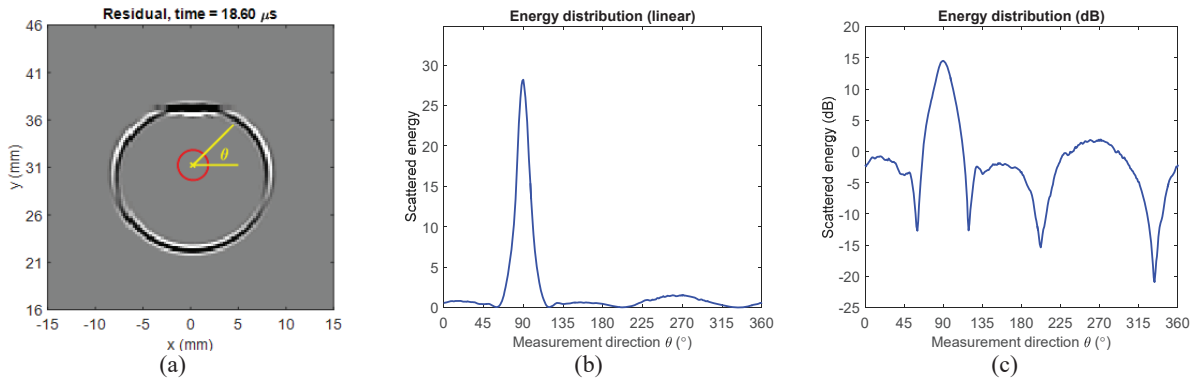

FIGURE 8. (a) Snapshot of the residual wavefield at 18.6 μs after space-time filtering. (b) Energy distribution of the second shear scattered skip on a linear scale, and (b) on a dB scale.
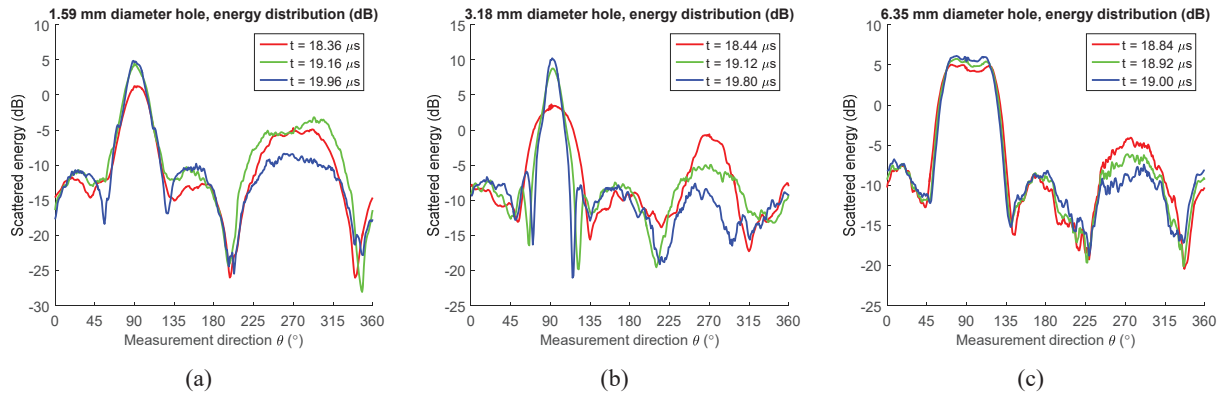
FIGURE 9. Scattered energy distribution of second shear scattered skip for a through-hole with a diameter of (a) 1.59 mm, (b) 3.18 mm and (c) 6.35 mm.

holes, the 1.59 mm hole has a broader forward lobe than the 3.18 mm hole as expected, conforming that a larger hole blocks more incident rays and leads to a narrower angle range of scattered waves; the largest hole (6.35 mm diameter) does not follow this trend, most likely because the scan area around the hole is more limited and it was not possible to quantify scattering very far from the hole.

SUMMARY AND CONCLUSIONS

This paper mainly shows that 3-D frequency-wavenumber filters and space-time filters are two effective tools that can be combined to isolate and characterize scattering of the primary shear wave skip. After filtering, scattering patterns are described as energy curves; i.e. scattered energy versus measurement direction, that are directly acquired from filtered ultrasonic wavefield data at specific times. In this way, detailed information is provided about how the distribution of shear wave scattered energy evolves with time. For scattering patterns among three different hole sizes of interest, the general shape of the scattered energy distribution is not a strong function of time for any of the holes. But for all three holes, the trend is still clear that the backscattered energy decreases and the forward scattering (shadowing effect) increases with time. Future work should address extending this methodology to more complicated scatterers.

ACKNOWLEDGMENTS

REFERENCES

1. J. Krautkrämer and H. Krautkrämer, *Ultrasonic Testing of Materials*, 2nd Edition, Springer-Verlag, New York, 1977.
2. P. J. Shull, ed,. *Nondestructive Evaluation: Theory, Techniques, and Applications*. New York: Marcel Dekker, 2002.
3. A. J. Dawson, J. E. Michaels, R. L. Levine, X. Chen, and T. E. Michaels, "Acquisition and analysis of angle-beam wavefield data," *Review of Progress in Quantitative Nondestructive Evaluation*, **33B**, D. E. Chimenti, L. J. Bond, and D. O. Thompson (Eds.), AIP Conf. Proc. **1581**, pp. 1716-1723, 2014.
4. A. J. Dawson, J. E. Michaels, and T. E. Michaels, "Isolation of ultrasonic scattering by wavefield baseline subtraction," *Mechanical Systems and Signal Processing*, **70-71**, pp. 891-903, 2016.
5. M. Ruzzene, "Frequency-wavenumber domain filtering for improved damage visualization," *Smart Materials and Structures*, **16**, pp. 2116-2129, 2007.
6. T. E. Michaels, J. E. Michaels, and M. Ruzzene, "Frequency-wavenumber domain analysis of guided wavefields," *Ultrasonics*, **51**, pp. 452-466, 2011.